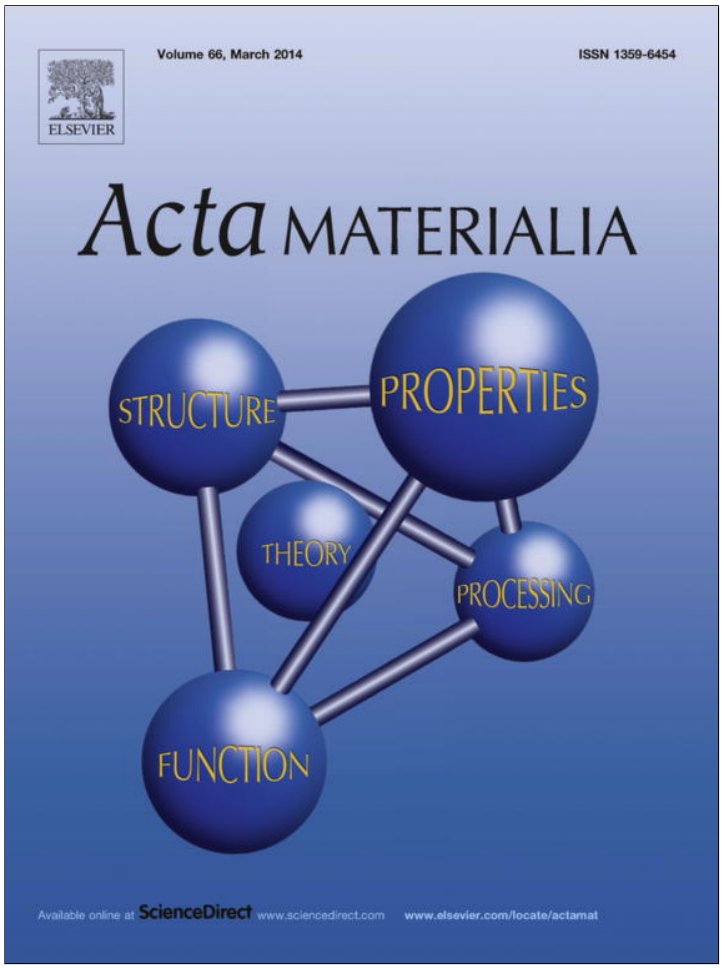

Available online at www.sciencedirect.com

ScienceDirect

Acta Materialia 66 (2014) 22–31

Acta MATERIALIA

www.elsevier.com/locate/actamat

Self-toughening crystalline Cu/amorphous Cu–Zr nanolaminates: Deformation-induced devitrification

J.Y. Zhang, G. Liu *, J. Sun *

State Key Laboratory for Mechanical Behavior of Materials, Xi'an Jiaotong University, Xi'an 710049, People's Republic of China

Received 17 August 2013; accepted 20 November 2013
Available online 28 December 2013

Abstract

How to defeat the conflict of strength vs. toughness and achieve unprecedented levels of damage tolerance within either metallic crystalline or metallic glassy family is a great challenge for designing structural materials. The combination of glassy with crystalline nanolayers can manifest extraordinarily high toughness, i.e. superior strength in conjunction with high ductility, when the constituent layers approach a critical internal feature size. Three-point bending and uniaxial microcompression tests were performed on Cu/Cu–Zr crystalline/amorphous nanolaminates (C/ANLs) with equal layer thicknesses ~50 nm to investigate their toughening behaviors. The dislocations absorbed by the amorphous phase not only render defect-free nanocrystals, but also create nanocrystallites in glassy nanolayers. It is revealed that the Cu/Cu–Zr C/ANLs self-toughen via the combination of the extrinsic shielding effect of crystalline/amorphous interfaces on a crack growth accommodated by an extensive shear-band sliding process and the intrinsic deformation-induced devitrification mechanism associated with the brittle-to-ductile transition of glassy nanolayers. The findings indicate that the high damage tolerance potentially accessible to glassy materials can extend beyond the benchmark ranges towards levels previously inaccessible to metallic crystalline–amorphous composites.

Keywords: Crystalline/amorphous nanolaminates; Interfaces; Dislocations; Fracture behavior; Crystallization

1. Introduction

The simultaneous attainment of high strength and great toughness/ductility is a vital requirement for most metallic structural materials, regardless of whether these are crystalline or glassy; unfortunately, these properties are generally mutually exclusive [1,2]. Crystalline materials exhibit ordered structures with morphological features (e.g. grains) that usually extend to the microscopic level. The well-defined dislocations—line defects associated with these internal features—become mobile under low stresses (<~1.3 GPa for Cu [3,4]), enabling extensive plastic shielding ahead of an opening crack, which benefits high toughness/ductility [5,6]. In contrast, metallic glasses (MGs) with an amorphous nature lacking microstructural defects could potentially yield plastically at much higher stresses (>~1.7 GPa [7–9]) via the shear transformation zones (STZs) [10–12]. Owing to the absence of these line defects, however, the attainable plasticity ahead of an opening crack tip is limited and, consequently, a catastrophic failure is usually accommodated by instantaneous propagation of the shear bands (SBs), leading to low toughness/ductility [5,6].

Ductile metals toughen mainly through intrinsic mechanisms, which are closely correlated with the microstructure-related plasticity [1,2]. However, brittle MGs toughen mainly through extrinsic mechanisms, which are primarily associated with resisting cracks propagation [1,2]. Artificial layering of materials to enhance fracture properties in mechanical applications has rapidly gained increasing interest because of the enhanced capability to tailor the

* Corresponding authors. Tel.: +86 (0)2982667143; fax: +86 (0)2982663453.
E-mail addresses: lgsammer@mail.xjtu.edu.cn (G. Liu), junsun@mail.xjtu.edu.cn (J. Sun).

1359-6454/$36.00
http://dx.doi.org/10.1016/j.actamat.2013.11.061

fabrication of these laminated architectures to satisfy specific needs [13–19]. Interestingly, numerous results [7,20–22] have unambiguously demonstrated that the crystalline/amorphous nanolaminate (C/ANL) architecture is a viable route towards developing materials with damage tolerance beyond those achievable from the constituents and vastly superior to those predicted from the simple rule of mixtures. Most recently, it is reported that the C/ANLs exhibit the maximum ductility at a critical layer thickness (h) ~25 nm accompanied by superior strengths [23–25], similarly to those of Cu/X (X = Cr, Nb, Zr) crystalline/crystalline nanolaminates (C/CNLs) [17,26]. The Cu/Cu–Zr C/ANLs also exhibit extraordinary tensile ductility ~4–14% [20,22], far greater than the reported values (~1–3%) of Cu/X (X = Ag, Cr, Nb, Zr) C/CNLs [17,26–29]. It is thus expected that the combination of amorphous with crystalline nanolayers can display extraordinarily high damage tolerance via extrinsic toughening mechanisms that have no effect on a crack initiation. Although significant efforts have been dedicated to studying the fracture behaviors of C/CNLs [17,26,30], the underlying fracture mechanisms of C/ANLs and the roles that crystalline/amorphous interfaces (CAIs) play in plasticity and fracture have not been addressed explicitly. Also, the MGs are not in thermodynamic equilibrium: supplying such materials with sufficient energy can stimulate the amorphous-to-crystalline transformation [31]. Mechanical energy in the form of plastic deformation can thus trigger the crystallization observed in several monolithic MGs (e.g. Al-based [32], Zr-based [33] and CuZr-based [34,35]), which is well known as deformation-induced devitrification (DID). For monolithic MGs, DID can improve their ductility as the localized shearing would be effectively impeded by crystallites [35–37], implying that these MGs can be toughened. However, the evolution of internal features in glassy layers and its effect on the deformation and fracture of C/ANLs have not been comprehensively understood.

The present work reports that the CAIs hinder crack propagation accompanied by crystallization of glassy nanolayers in three-point bending deformation of the Cu/Cu–Zr C/ANLs, as is further verified in micro-compression tests. The self-toughening mechanisms in metallic C/ANLs are illustrated via the combination of CAI and DID blocking effects on the propagation of cracks/SBs, in addition to the brittle-to-ductile transition of glassy nanolayers.

2. Experimental details

2.1. Preparation and microstructure characterization of Cu/Cu–Zr nanolaminates

Cu/Cu–Zr nanolaminates ~2 μm thick with equal layer thickness (h) ~50 nm and monotonic $Cu_{60}Zr_{40}$ amorphous films were deposited on 1000-μm-thick (100)-Si substrates by direct current (DC) magnetron sputtering at room temperature. Cu (99.995%) and Zr (99.99%) targets were used to produce alternating layers of nanocrystalline (NC) Cu and amorphous $Cu_{60}Zr_{40}$ (atomic fraction). The internal structure features of as-deposited Cu/Cu–Zr C/ANLs were characterized by X-ray diffraction (XRD) and transmission electron microscopy (TEM). Detailed descriptions of the preparation of the multilayers and characterization of the microstructure have been described elsewhere [38].

2.2. Three-point bending test of Cu/Cu–Zr nanolaminates

Static three-point bending tests were conducted using a Micro-Force Test System (MTS® Tytron 250). The width of all specimens was 4.0 mm. The velocity of the loading head was 0.1 mm min^{-1}. To ensure substrate cracking prior to multilayer fracture and to minimize deformation of the top surface of the nanolaminate, the brittle 1000 μm thick Si substrate was deliberately scratched near the two ends (forming some microcracks), and the bending span was set at 40 mm, as shown schematically in Fig. 1. In the present work, the stress non-homogeneity effect of an opening crack tip can be eliminated, because the multilayer-to-substrate thickness ratio is ~1/500 [30]. Subsequently, TEM samples were fabricated by focused ion beam (FIB) from the cracked regions in the bent samples using a trenching and lift-out technique. However, it is difficult to obtain an accurate force–displacement curve of the cracked region in the three-point bending test, and it does not allow for an accurate assessment of the intensity of stress field of an opening crack tip (ISFT) in the present multilayer/substrate system.

2.3. Microcompression test of Cu/Cu–Zr micropillars

To further explore their micro-scaled mechanical properties, microcompression tests were performed, which enables the magnitude of ISFT to be roughly estimated/assessed by obtaining the true stress–strain curves (simply assume the ISFT equals the maximum strength σ_{max}) of Cu/Cu–Zr nanolayered micropillars. The small tapered (~2°) Cu/Cu–Zr micropillars with diameter (ϕ) ~950 nm were fabricated from the as-deposited multilayers using a Helios Nano Lab 600i dual-beam FIB system, which also allows scanning electron microscopy (SEM) observations. All the pillars were then uniaxially compressed in a Hysitron Ti 950 with a 10 μm side-flat quadrilateral cross-section diamond indenter at a constant strain rate ($\dot{\varepsilon}$) of 2×10^{-4} s^{-1} up to ~20–30% strain. After accounting for

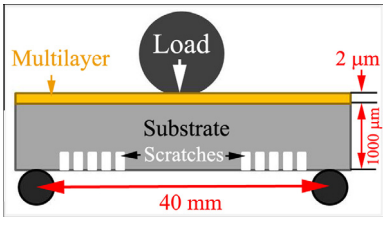

Fig. 1. Schematic illustration of the three-point bending apparatus used for the localized fracture experiment.

the substrate effects and correcting for tapers, the true strain (ε_T) and true stress (σ_T) are given by [7]:

$$\varepsilon_T = \frac{1}{E_m}\frac{PL_p}{A_0L_0} + \ln\left(\frac{L_0}{L_p}\right) = \frac{1+\frac{L_0}{r_0}\tan\psi}{E_{measured}}\frac{PL_p}{A_0L_0} + \ln\left(\frac{L_0}{L_p}\right) \quad (1)$$

and

$$\sigma_T = \frac{P}{A_p} = \frac{PL_p}{A_0L_0} = \frac{P}{A_0L_0}\left\{L_0 - \left[u_{tot} - \frac{PL_{Si}}{E_{Si}A_{Si}} - \frac{\sqrt{\pi}P(1-v_m^2)}{2E_{Si}\sqrt{A_{Si}}}\right]\right\} \quad (2)$$

where A_0 is the cross-sectional area at half the initial height (L_0) of the pillar, r_0 is the radius at the pillar top, L_p and A_p are the final height and average cross-sectional areas, respectively, P is the applied load, E_m is the true modulus of Cu/Cu–Zr pillars without tapers, and $E_{measured}$ is the measured modulus of tapered Cu/Cu–Zr pillars following the treatment of Knorr et al. [39], u_{tot} is the total displacement, v_m is the Poisson's ratio of Cu/Cu–Zr nanolaminates (~0.33), and A_{Si}, L_{Si} and E_{Si} are the average cross-sectional area, the total length and the modulus of the Si substrate, respectively. More details about the pillars preparation and compression procedures can be found in Ref. [7].

3. Results

3.1. Microstructure features

Cross-sectional microstructures of the Cu/Cu–Zr C/ANLs were examined in detail by high-resolution TEM (HRTEM), as typically displayed in Figs. 2 and 3, from which one can see the modulated layer structures. Some growth nanotwins parallel to the CAIs are observed in NC Cu nanolayers, while glassy $Cu_{60}Zr_{40}$ nanolayers exhibit an amorphous nature. The selected-area diffraction patterns (SADPs) reveal a strong (1 1 1) peak in NC Cu layers and an amorphous nature in glassy $Cu_{60}Zr_{40}$ layers, consistent with the XRD results. More details can be found in previous work [7,38].

3.2. Bending fracture behavior

To elucidate the fracture behaviors of Cu/Cu–Zr C/ANLs under three-point bending tests, the localized deformation features in the cracking zones were examined in detail by HRTEM observations, as shown clearly in Figs. 2 and 3. From these images, the following sequences are proposed for crack propagation/growth.

(i) The crack that initiates from the substrate penetrates through the Cu seed layer, propagates within the first glassy layer and blunts to some extent at the interface/twin boundary (see Fig. 2d). However, the ISFT is still large enough to result in the cracking of the next glassy layer, accompanied by deformation (i.e. dislocation activities) in the first NC Cu layer.

(ii) The crack re-sharpens in the second glassy layer, overcomes the blocking effect of an interface and that of NC Cu (Cu nanolayer shows intragranular fracture; see Fig. 2c), propagates within the third glassy layer, reaches the interface and blunts once again (see Fig. 2b).

(iii) The sharply reduced ISFT cannot outstrip the suppression effect of the NC Cu layer, but definitely causes the deformation of the Cu layer, leading to shear in an adjacent glassy layer (see Fig. 2b).

(iv) The sheared zone (i.e. crack) is so small or the ISFT is so weak that the crack is finally arrested by the interface (or Cu layer) after transmitting across three modulation periods (see Fig. 2a). Furthermore, one can see in Fig. 2a that the crack propagation path inclines to the multilayer/substrate interface with an angle $\theta \approx 66°$, similarly to those of $h = 50$ nm stretched Cu/X (X = Cr, Nb, Zr) [17,40] and Cu/Cu–Zr [24,25] nanolaminates. Also, it appears in Figs. 2 and 3 that the intragranular shear fracture occurs in Cu nanolayers without significant thinning, which is different from the intergranular shear fracture and necking of Cu layers observed in h = 50 nm Cu/Au and Cu/Cr C/CNLs [30].

To sustain plastic deformation of the present Cu/$Cu_{60}Zr_{40}$ samples, the basic mechanisms of dislocations and/or twinning for the NC layers [41–43] and SB or STZ for the amorphous layers [44–46] should be considered at such length scale, as well as the interactions between the amorphous and crystalline nanolayers. Interestingly, no dislocation pile-up and/or accumulation, and no planar defects (e.g. stacking faults and deformation twins) are observed in the deformed NC Cu layers. Another interesting feature is that lots of nanocrystallites with sizes of ~1.5–4.5 nm are frequently observed at two sides of a crack in the deformed glassy layers, as shown in Fig. 3f and g. However, under stretched conditions, the DID process is not observed in the ~14% stretched 35 nm Cu/5 nm $Cu_{75}Zr_{25}$ C/ANL reported by Wang et al. [20] and ~4% stretched 16 nm Cu/(17–112) nm $Cu_{50}Zr_{50}$ C/ANL reported by Kim et al. [22]. These findings indicate that layer geometries, loading modes and deformation magnitudes can significantly affect the amorphous-to-crystallization transition in glassy materials, in addition to their intrinsic properties such as composition and thermal stability.

3.3. Compressive flow behavior

Typical true stress–strain curves of the Cu/Cu–Zr pillars imposed at two different strains (~20%, 30%) are shown in Fig. 4a. It is found that the Cu/Cu–Zr pillars exhibit smooth plastic flow, which is in sharp contrast to the jerky true stress–strain response of pure amorphous pillars (see

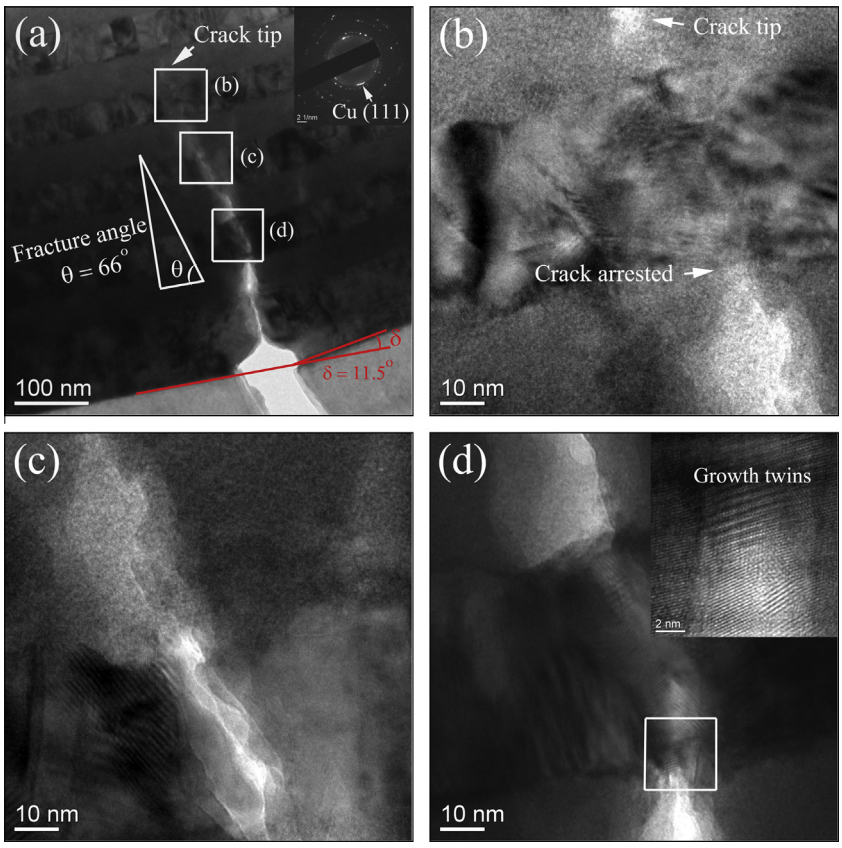

Fig. 2. (a) Typical TEM images of $h = 50$ nm C/A multilayers fractured with angle ~66°. Inset in (a) is the SADP that reveals strong Cu (1 1 1) texture in the Cu layer. (b–d) Magnified views of boxed regions in (a): (b) the crack is arrested at the interface; (c) the crack overcomes the blocking effect of NC Cu layer and propagates in the amorphous layer; and (d) the crack is arrested at the twin boundaries and blunted. Inset in (d) is the magnified image of boxed region showing growth nanotwins.

Fig. 4b), supporting the absence of shear banding events often associated with monolithic MGs. Specifically, the true stress–strain response of the Cu/Cu–Zr pillar gradually shifts from initial strain hardening (at low plastic strains $\varepsilon_p < 10\%$) to work softening (at high plastic strains $\varepsilon_p > 10\%$). Furthermore, the maximum strength of Cu/Cu–Zr pillar is $\sim 2.1 \pm 0.15$ GPa, and the yield strength of amorphous is $\sim 1.7 \pm 0.05$ GPa.

A typical FIB/SEM image of a ~20% compressed Cu/Cu–Zr pillar with $h = 50$ nm is shown in Fig. 5a. It appears that the deformed sample shows plastic barreling and extrusion of Cu instead of shear banding [7]. A cross-sectional micrograph of this ~20% strained pillar displayed in Fig. 5b shows that neither shear fracture nor interfacial delamination is observed in the glassy layers, even though its maximum strength far overwhelms the yield strength of the amorphous pillar. Further cross-sectional FIB/SEM observations reveal that, though the deformation is not homogeneous at the upper part of the pillar, the layered structure remains intact (see the rectangle region in Fig. 5b), presumably because of the slightly smaller diameter and higher stresses at the top; but the lower layers near the substrate show no measurable plastic strain. These are in good agreement with the observations on Cu/Pd–Si by Knorr et al. [39] and in Cu/Zr–Cu by Liu et al. [47].

In contrast, it is found in the ~30% compressed Cu/Cu–Zr pillar that the wave-like CAIs, involving a non-uniform reduction in layer thickness and breakage of glassy layers, is radically different from the relative homogeneity in deformation in the 20% strained sample; see Fig. 5c and d. This means that the heterogeneity in the layer thickness reduction as well as the breakage of glassy layers is only apparent under such severe deformation (~30% strain). To further explore the evolution of the internal features of deformed Cu/Cu–Zr micropillars and to unveil the corresponding deformation mechanism, TEM samples were fabricated by FIB from 30% deformed Cu/Cu–Zr micropillar through-thickness cross sections, as shown in Fig. 6a. The findings from TEM observations are summarized as follows: (i) there is no interfacial delamination, in addition to the non-uniform thickness reduction, consistent with SEM/FIB observations (see Fig. 5); (ii) there are no traces of fracture or microcracks in the NC Cu and amorphous Cu–Zr layers; (iii) neither heavy dislocation storage nor abundant planar defects such as stacking faults and deformation twins in the NC Cu (and crystallized Cu–Zr amorphous) layers are observed, in good agreement with the bending test results; (iv) the glassy Cu–Zr layers are almost fully crystallized, forming ~10–50 nm nanosized orthorhombic $Cu_{10}Zr_7$ crystallites rather than SB. Also, ultrafine

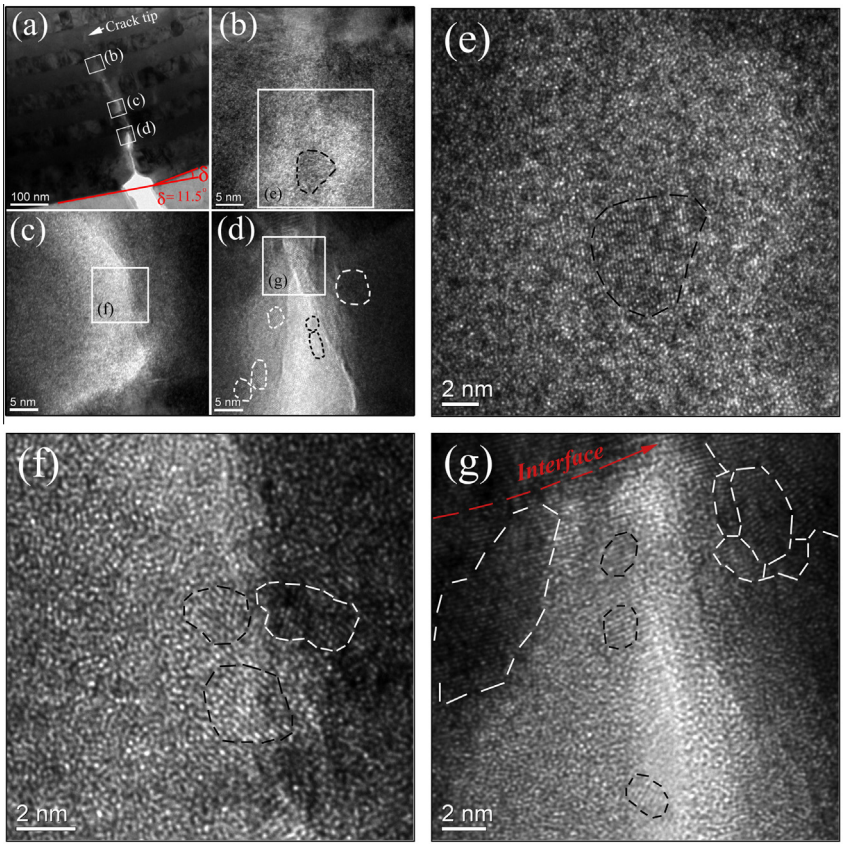

Fig. 3. (a) Typical TEM images of $h = 50$ nm C/A multilayers. (b–d) Magnified view of boxed region in (a). (e) Magnified image in (b); (f) magnified image in (c); (g) magnified image in (d), showing nanocrytallites in amorphous layers as indicated by dashed circles.

nanocrystallites with sizes of ~1–3 nm in the residual amorphous region are frequently observed.

4. Discussion

4.1. Size-dependent fracture behavior in Cu/Cu–Zr C/ANLs

To provide a context for this size-dependent fracture behavior, it is useful to consider the fracture process as a conflict: in fracture mechanics terms, as a mutual competition between what can be termed intrinsic damage mechanisms, which promote crack advance, and extrinsic crack-tip-shielding mechanisms, which impede crack advance [1,5]. If the crack tip encounters an interface, the capability of a crack propagation is critically related to how the structure is able to transfer the stress at the tip to the next brittle layer [5]. Therefore, the suppression of crack propagation can effectively enhance the ductility/toughness of nanolaminates. Whether the cracks can be suppressed is dependent on two opposite, competing factors [17,26,48]. One is the intrinsic damage-related ISFT, which scales with the crack size or length [26]. This would lead to the expectation that a small crack is unfavorable for its growth, thereby enhancing a material's ductility/toughness. The other is the extrinsic shielding on crack propagation accommodated by plastic deformation (dislocation activities) in NC Cu, which becomes rather limited when the layer is too thin [26]. This renders the ductile-to-brittle transition in NC Cu nanolayers and weakens their capability in resisting crack growth, thereby undercutting a material's ductility/toughness. This mutual competition between intrinsic and extrinsic toughening mechanisms determines the h-dependent fracture behavior [17,26,48]. Also, in previous work [17,26,48], the present authors demonstrated that, for the ductile/brittle C/CNLs, the fracture angles are determined mainly by the geometries (i.e. layer thickness) of multilayers. As h is below ~60–100 nm, the ISFT is sharply decreased, which renders the shear fracture with angle $\theta \approx 66°$ [17].

4.2. Size-dependent brittle-to-ductile transition of glassy layers in Cu/Cu–Zr C/ANLs

Molecular dynamics (MD) simulations [49,50] as well as experimental results [51,52] indicate that plastic deformation in a homogeneous-like fashion is possible at least for some MGs. For example, when the sample dimension is larger than the critical size ~60–100 nm [7,22], the materials fail by SB propagation without notable plasticity, but below this critical size, the homogeneous plastic deformation precedes the SB propagation, showing significant plasticity [7,21,22,51,52]. This implies that, as the characteristic

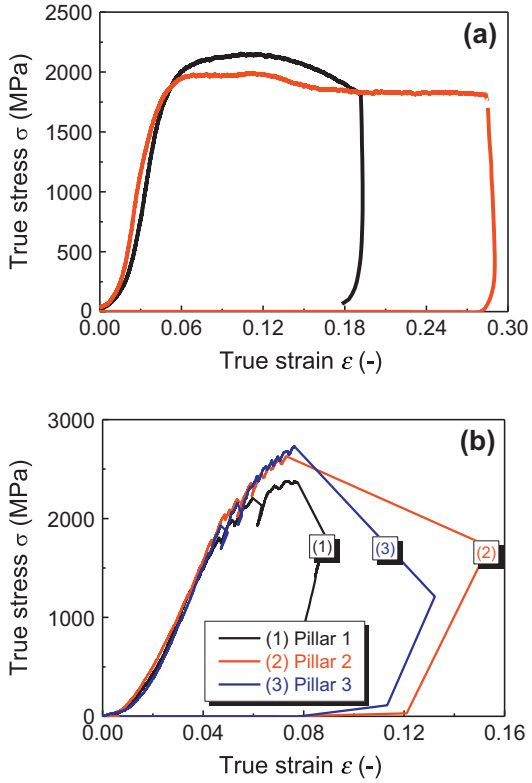

Fig. 4. (a) True stress–strain curves for the Cu/Cu–Zr micropillars compressed at different strains (~20% and 30%); (b) true stress–strain plots for the monolithic amorphous micropillars.

dimensions of MG are reduced to a nanoregime, smaller samples show homogeneous extension rather than the highly localized plasticity (i.e. shear banding) in larger ones [7,21,22,51,52]. Also, as can be seen in the present micro-compression tests, the glassy Cu–Zr nanolayers exhibit the capability of homogeneous plasticity without instantaneous catastrophic failure. The basic premise for small-sized MGs to be capable of displaying homogeneous plasticity is that their internal structures contain sufficient STZs that can be a driven by the applied stresses to participate in shear transformations, so that a high "deformation participation ratio" [49,53] alleviates the severe concentration of strain into thin SBs [8,9]. In this case, STZs and groups thereof may self-organize into a network rather than into a SBs, and shear banding becomes "nucleation controlled" at the outset of its formation in these small-sized samples [8,9,51,52]. Therefore, in the present case ($h = 50$ nm), shear banding becomes so unfavorable that it subsides altogether and gives way to STZ operation everywhere, leading to homogeneous plasticity of the samples. Specifically, the spread-out STZ actions, i.e. some homogeneous-like plastic flow, are more obvious under the confinements imposed in the compression tests [8,9,54] and the constraining conditions and/or extremely small length scales [7,20–22,39]. In addition, at such a length scale ($h = 50$ nm), though the SBs can form via activation of the STZs eventually, they are difficult to propagate in glassy nanolayers because of the constraining effects of the strong NC Cu nanolayers [7]. Therefore, refining the thickness of glassy nanolayers (to achieve the brittle-to-ductile transition) in C/ANLs is a viable (intrinsic) toughening route towards developing materials that combine high strengths with great deformability [21,22].

4.3. Deformation mechanisms in Cu/Cu–Zr C/ANLs

Here, the underlying mechanisms for the lack of abundant residual defects (e.g. dislocations, stacking faults and deformation twins) are elucidated, and the focus is mainly on the mechanism of atomic arrangements in the DID behavior from the following atom-scale perspective. Recent MD simulations have revealed that (leading and trailing) partials/full dislocations are observed in the Cu nanolayers, and screw dislocations are seen near the CAI in $Cu/Cu_{46}Zr_{54}$ C/ANLs [55]. Further experimental observations and MD simulations have demonstrated that the glassy nanolayers (or the CAIs) not only exhibit the extraordinary capacity to act as effective barriers for dislocations, but also as dislocation sources/sinks, enabling absorption of free volumes and free energy transported by the dislocations through CAIs [20,55]. When the incoming dislocations transmit across the CAIs and propagate inside the isolated Cu nanolayer, they will be absorbed by the opposite CAIs (into the amorphous layer), leaving no dislocation debris [56,57]. Specifically, the trailing partials emitted from sources can effectively erase the stacking faults created by the leading partials, which lowers the density of stacking faults/twins in crystals and manifests the absence of abundant defects [43].

On the one hand, the glassy layers can significantly affect dislocation structures by the attraction/annihilation of dislocations, thereby sharply reducing the dislocation density in NC nanolayers [7,20]. This leads to work-softening in the samples at great strains, consistent with the true stress–strain curves. On the other hand, once these dislocations hit on or glide along CAIs, they will activate STZs in a correlated fashion near the intersection line between the dislocation slip plane and CAIs without significant atomic rearrangements in its surrounding glassy matrix [20,55]. They subsequently activate other STZs nearby, and gradually gain correlation both temporally and spatially [12,20,58]. In other words, once the STZs are created by the absorbed dislocations, these activated STZs will "infect" their surrounding STZs to propagate, similarly to the stimulated dislocations slip [41,59] in crystals. In the present experiments, the small layer thickness makes it difficult for STZs and groups thereof to self-organize into a larger flow zone and to reach the threshold that would trigger the self-sustaining shear banding, as mentioned above. Because the activations of individual STZs are independent of each other under mechanical stresses at room temperature [36,58,60], interactions between these activation units of plastic flow in the glassy layers are thus impossible to alter the plastic mechanism in the consecutive

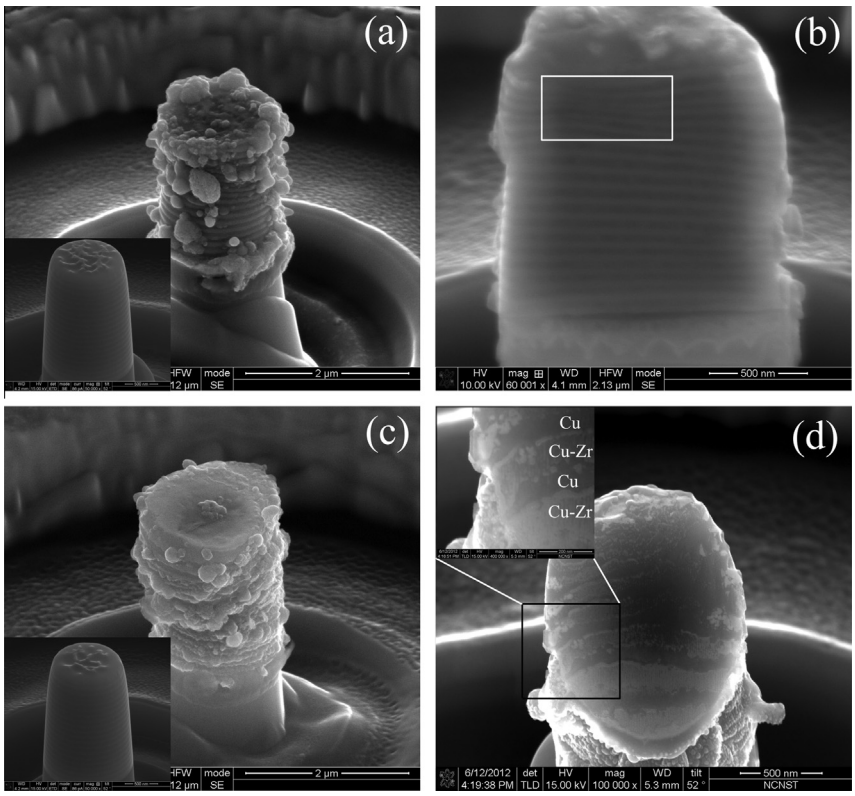

Fig. 5. (a) SEM micrograph showing the Cu/Cu–Zr pillar compressed to ~20% strain accompanied by barreling and extrusion of Cu. Inset is the as-milled pillar. (b) Cross-sectional image of the FIB-ed deformed pillar (with direction perpendicular to the top surface of the pillar), showing the layered structure and uniformly thinned Cu layers; (c) SEM micrograph showing the Cu/Cu–Zr pillar compressed to ~30% strain accompanied by barreling and extrusion of Cu. Inset is the as-milled pillar. (d) Cross-sectional image of the FIB-ed deformed pillar (with 45° direction to the normal of the pillar top surface), showing heterogeneity in the layer thickness reduction and the breakage of glassy layers. Inset is the magnified view of boxed region in (d).

deformation. The formation of nanocrystallites is thus closely linked to the localized shear flow, i.e. STZ-mediated activities. In addition, Chen and coworkers [36,58] pointed out that the STZs can serve as the embryos for DID in an embryonic SB. The present authors thus suspect that, owing to dislocation absorption, these localized regions of atomic displacements/rearrangements (i.e. STZs) would be likely to trigger the nucleation of crystalline nuclei, which grow to form nanocrystallites (i.e. DID). Specifically, these nanocrystallites interact with the SBs to hinder their propagation [36,61]. To sustain a deformation rate in a sample during mechanical tests, new STZs or SBs need to be generated when the active SBs are blocked by these nanocrystallites. Therefore, DID is another main source of intrinsic toughening against initiation and propagation of cracks, elevating the material's inherent damage tolerance.

It should be pointed out that DID in the present Cu/Cu–Zr C/ANLs differs considerably from that observed in monolithic CuZr-based bulk amorphous materials [35,36]. For the former, the crystallization is stimulated via absorption of dislocations, even in slight deformation (e.g. the bending angle δ is ~11.5°), while DID is only observed inside the highly localized SBs for the latter. It is suggested that absorbed dislocations more effectively promote crystallization in glassy layers, which tunes their inherent damage tolerance by changes in the microstructure. Specifically, the Cu/Cu–Zr pillars display superior deformability ~30%, and simultaneously maintain superior strengths ~2 GPa.

4.4. Mechanisms of DID in Cu/Cu–Zr C/ANLs

The question is naturally raised of why and how the amorphous-to-crystallization transition occurs during the propagation of a crack in glassy nanolayers at room temperature even without either significant large deformation associated with mass transportation [33] or shear-banding-induced temperature rise [62] in the present case. To understand the underlying reason for DID, the present authors follow the spirit of Lu [31], similarly to Lee et al. [35], in terms of the viewpoints of thermodynamics and kinetics associated with two different stress states imposed on the samples, i.e. hydrostatic compression and shear. When the uniaxial compression of ~2 GPa (corresponding to the maximum strength of present C/A samples) is applied to the sample, it is decomposed into hydrostatic compression (~0.67 GPa) and shear stress (~1 GPa) at the maximum shear plane. The hydrostatic compressive stress reduces the energy barrier for nucleation, while the

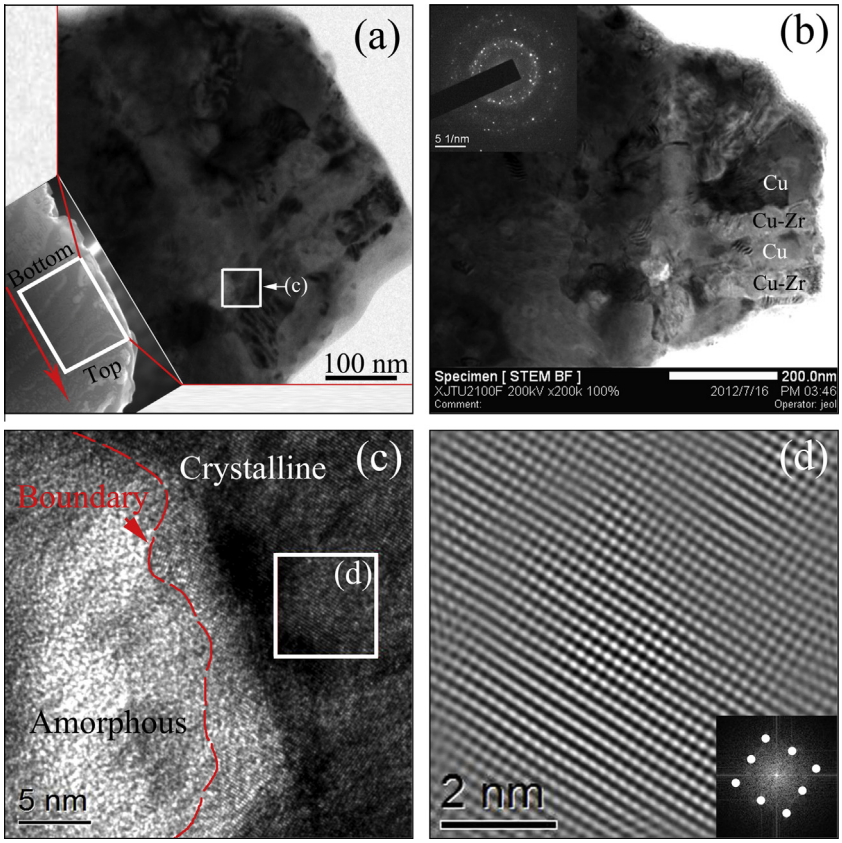

Fig. 6. (a) Typical TEM image of a ~30% compressed Cu/Cu–Zr micropillar with $h = 50$ nm. Inset is the cross-sectional SEM image of the deformed pillar, schematically representing the orientation of the FIB-ed TEM sample. (b) Low-magnification STEM image of (a), demonstrating a chemically alternating layer structure of the deformed micropillars and showing deformation heterogeneity; inset is the corresponding SADP of (b). (c) Magnified TEM image of boxed area in (a), showing residual amorphous region and crystallization in a glassy layer. The red dashed line indicates the boundary between the crystalline and amorphous regions. (d) Inverse fast Fourier transform (FFT) HRTEM image of boxed area in (c) and the corresponding FFT pattern (inset), showing crystalline $Cu_{10}Zr_7$ phase. (For interpretation of the references to color in this figure legend, the reader is referred to the web version of this article.)

shear stress lowers the energy barrier for diffusion and induces the atoms to migrate along the shearing direction, facilitating an increase in the local free volumes associated with atomic dilatation [35,63]. Therefore, the simultaneous action of hydrostatic compression and shear stress via uniaxial compression induces an enhancement of the nucleation rate, which promotes crystallization to accommodate the external compressive stress by reducing the volume of the amorphous phase through crystallization at room temperature.

The STZ-mediated activities, i.e. cooperative shearing of unstable STZs activated by dislocations, is the underlying reason for achieving the DID as well as the homogeneous-like flow in glassy Cu–Zr nanolayers, as analyzed above. As the same fundamental processes are required to maintain plastic flow as for DID, namely atomic rearrangements, here the mechanisms underlying the precipitation of orthorhombic $Cu_{10}Zr_7$ nanocrystals on deformation are qualitatively elucidated, following the idea of cooperative shearing model [64]. Viscosity η can be expressed as [61,65]:

$$\eta = \eta_0 \exp\left[\frac{\Delta F(T) + \alpha(\beta W - E_{\text{los}} + E_{\text{dis}})}{k_B T}\right] = \eta_0 \exp\left[\frac{\Delta G(T)}{k_B T}\right] \quad (3)$$

where the pre-exponential constant η_0 is the viscosity at infinite temperature; T is the temperature; k_B is the Boltzmann constant; $\Delta F(T)$ is the temperature-dependent activation energy; $W = \int_0^{\varepsilon} \sigma d\varepsilon$ stands for strain energy of the sample per unit volume (i.e. the energy used to stretch/compress the sample up to a particular strain value, equivalent to the area covered by the true stress–strain curve from $\varepsilon = 0$ to the particular strain or the integral from 0 to the particular strain); α is a coefficient; β is the contribution of crystalline layers to the total strain of the present samples (roughly taking $\beta \approx 0.5$); E_{los} is the lost energy during deformation; and E_{dis} is the self-energy of N dislocations ($N = (\pi\varepsilon\phi^2)/(4b\lambda)$) contributing to DID, which can be simply assessed by [66,67]: $E_{\text{dis}} = N\frac{Gb^2}{2\pi(1-\nu_{\text{Cu}})}\left[\ln\left(\frac{\lambda-b}{b}\right)+1\right]$, where G is the shear modulus of Cu (~45 GPa); b is the Burgers vector; ν_{Cu} is the Poisson ratio of Cu (~0.343); and λ is

the dislocation slip distance scaling with h. The potential energy can be expressed by a sinusoidal function similar to the function used to describe the theoretical shear strength of crystalline solids [68], $Q/Q_0 = \sin^2[(\pi\gamma)/(4\gamma_c)]$, where Q is the potential energy, Q_0 is the amplitude of the energy function, γ is the shear strain, and γ_c is a critical shear strain limit. The second derivative of the potential energy with respect to the shear coordinate (representing the curvature of the potential energy function at $\gamma = 0$) gives the instantaneous shear modulus G^* [64]:

$$\frac{d^2Q}{d\gamma^2}|_{\gamma=0} = G^* = \left(\frac{\pi^2}{8\gamma_c^2}\right)Q_0 \tag{4}$$

Given the contribution of crystalline layers, the total barrier height for the stress-assisted, thermally activated process $\Delta G(T)$, which is the product of the amplitude of the potential energy function (Q_0) and the size of the cooperatively rearranging zone (Ω), can be written as:

$$\Delta G(T) = \Delta F(T) + \alpha\left(\beta\int_0^{\varepsilon}\sigma d\varepsilon - E_{los} + E_{dis}\right) = Q_0\Omega = \frac{8\gamma_c^2}{\pi^2}G^*\Omega \tag{5}$$

Eq. (5) correlates the barrier height with G^* and Ω, and provides the basis for the following discussion. It signifies that, at a given strain, $\Delta G(T)$ decreases if G^* decreases or if Ω is still small and, consequently, flow is facilitated. When mechanical energy is introduced into the system, shearing has been found to flatten out the less stable local minima in the potential energy landscape (inherent states) and eventually to let them vanish completely, which is equivalent to a significant local softening of G [61,69]. That is to say, the mechanical stress triggers structural rearrangements by facilitating flow [70]. Without the assistance of long-range atomic diffusion in deformed regions, the precipitation of stable equilibrium phases $Cu_{10}Zr_7$ also indicates a possible structural affinity of the $Cu_{10}Zr_7$ phase and the glassy matrix on a short-range order length scale, and the DID process is kinetically favored [61]. The formation of $Cu_{10}Zr_7$ nanocrystals consumes energy, and their growth thus is expected to become more difficult for the larger sized crystals. This follows from Eq. (5), which states that the activation energy of flow is proportional to Ω. When more (deformation) energy is introduced into the system, the crystalline nuclei grow up/deform. In this regard, the precipitation of $Cu_{10}Zr_7$ nanocrystals and their subsequent growth/deformation are expected to relax stresses in the surrounding matrix and to reduce the likelihood of the formation of local entities in which structural rearrangements are concentrated [35,61]. The high density of nanocrystals limits SB extension and effectively prevents shearing by a "self-locking" effect, leading to great plasticity [36].

5. Summary

By investigating the bending fracture and compressive flow behaviors of C/A Cu/Cu–Zr multilayers/micropillars, the present authors illustrate the effects of CAIs and structural evolution on plastic deformation. The present results hopefully convey that the CANL architecture provides a viable way to attain highly damage-tolerant materials via a better combination of intrinsic toughening (DID and the brittle-to-ductile transition of glassy layers) and extrinsic toughening (CAI shielding) mechanisms, dealing with the conflicts between the generally mutually exclusive properties of strength and toughness in the MG composites. The absorption of dislocations by amorphous layers catalyzes DID via activation of the STZs, leaving no dislocations and planar defects in crystalline layers.

Acknowledgements

This work was supported by the National Natural Science Foundation of China (Grant Nos. 51321003, 51322104, 51201123), the 973 Program of China (Grant No. 2010CB631003), and the 111 Project of China (B06025). GL thanks the support from Fundamental Research Funds for the Central Universities and the Tengfei Scholar project. JYZ thanks China Postdoctoral Science Foundation (2012M521765) and Shaanxi Province Postdoctoral Scientific Research Projects for partial financial support. Access to the nanoindentation and FIB equipment in CAMP-Nano is also acknowledged.

References

[1] Ritchie RO. Nat Mater 2011;10:817–22.
[2] Hofmann DC, Suh JY, Wiest A, Duan G, Lind ML, Demetriou MD, et al. Nature 2008;451:1085–9.
[3] Dao M, Lu L, Asaro RJ, De Hosson JTM, Ma E. Acta Mater 2007;55:4041–65.
[4] Zhang JY, Zhang X, Liu G, Wang RH, Zhang GJ, Sun J. Mater Sci Eng A 2011;528:7774–80.
[5] Was GS, Foecke T. Thin Solid Films 1996;286:1–31.
[6] Demetriou M, Launey ME, Garrett G, Schramm JP, Hofmann D, Johnson WL, et al. Nat Mater 2011;10:123–8.
[7] Zhang JY, Liu G, Lei SY, Niu JJ, Sun J. Acta Mater 2012;60:7183–96.
[8] Wang CC, Ding J, Cheng YQ, Wan JC, Tian L, Sun J, et al. Acta Mater 2012;60:5370–9.
[9] Tian L, Shan ZW, Ma E. Acta Mater 2013;61:4823–30.
[10] Schuh CA, Hufnagel TC, Ramamurty U. Acta Mater 2007;55:4067–109.
[11] Falk ML, Langer JS, Pechenik L. Phys Rev E 2004;70:011507.
[12] Falk ML, Langer JS. Phys Rev E 1998;57:7192–205.
[13] Han SM, Phillips MA, Nix WD. Acta Mater 2009;57:4473–90.
[14] Wang J, Misra A. Curr Opin Solid State Mater Sci 2011;15:20–8.
[15] Zhang JY, Lei SY, Liu Y, Niu JJ, Chen Y, Liu G, et al. Acta Mater 2012;60:1610–22.
[16] Zhang JY, Lei S, Niu J, Liu Y, Liu G, Zhang X, et al. Acta Mater 2012;60:4054–64.
[17] Zhang JY, Zhang X, Wang RH, Lei SY, Zhang P, Niu JJ, et al. Acta Mater 2011;59:7368–79.

[18] Demkowicz MJ, Misra A, Caro A. Curr Opin Solid State Mater Sci 2012;16:101–8.
[19] Bhattacharyya D, Mara NA, Dickerson P, Hoagland RG, Misra A. Acta Mater 2011;59:3804–16.
[20] Wang YM, Li J, Hamza AV, Barbee JTW. Proc Natl Acad Sci USA 2007;104:11155–60.
[21] Kim JY, Gu X, Wraith M, Uhl JT, Dahmen KA, Greer JR. Adv Funct Mater 2012;22:1972–80.
[22] Kim JY, Jang DC, Greer JR. Adv Funct Mater 2011;21:4550–4.
[23] Huang HS, Pei HJ, Chang YC, Lee CJ, Huang JC. Thin Solid Films 2013;529:177–80.
[24] Lee CJ, Lin HK, Huang JC, Kuan SY. Scripta Mater 2011;65:695–8.
[25] Pei HJ, Lee CJ, Du XH, Chang YC, Huang JC. Mater Sci Eng A 2011;528:7317–22.
[26] Zhang JY, Liu G, Zhang X, Zhang GJ, Sun J, Ma E. Scripta Mater 2010;62:333–6.
[27] Zhang JY, Zhang X, Liu G, Zhang GJ, Sun J. Scripta Mater 2010;63:101–4.
[28] Mara NA, Bhattacharyya D, Hoagland RG, Misra A. Scripta Mater 2008;58:874–7.
[29] Huang H, Spaepen F. Acta Mater 2000;48:3261–9.
[30] Li YP, Zhang GP. Acta Mater 2010;58:3877–87.
[31] Lu K. Mater Sci Eng R: Rep 1996;16:161–221.
[32] Chen H, He Y, Shiflet GJ, Poon SJ. Nature 1994;367:541–3.
[33] Kim JJ, Choi Y, Suresh S, Argon AS. Science 2002;295:654–7.
[34] Lee JC, Kim YC, Ahn JP, Kim HS, Lee SH, Lee BJ. Acta Mater 2004;54:1525–33.
[35] Lee SW, Huh MY, Fleury E, Lee JC. Acta Mater 2006;54:349–55.
[36] Chen MW, Inoue A, Zhang W, Sakurai T. Phys Rev Lett 2006;96:245502.
[37] Das J, Tang MB, Kim KB, Theissmann R, Baier F, Wang WH, et al. Phys Rev Lett 2005;94:205501.
[38] Zhang JY, Liu Y, Chen J, Chen Y, Liu G, Zhang X, et al. Mater Sci Eng A 2012;552:392–8.
[39] Knorr I, Cordero NM, Lilleodden ET, Volkert CA. Acta Mater 2013;61:4984–95.
[40] Zhang JY, Zhang X, Liu G, Zhang GJ, Sun J. Mater Sci Eng A 2011;528:2982–7.
[41] Zhang J-Y, Liu G, Wang RH, Li J, Sun J, Ma E. Phys Rev B 2010;81:172104.
[42] Zhang JY, Zhang P, Wang RH, Liu G, Zhang GJ, Sun J. Phys Rev B 2012;86:064110.
[43] Zhu YT, Liao XZ, Wu XL. Prog Mater Sci 2012;57:1–62.
[44] Greer JR, De Hosson JTM. Prog Mater Sci 2011;56:654–724.
[45] Wang WH. Prog Mater Sci 2012;57:487–656.
[46] Trexler MM, Thadhani NN. Prog Mater Sci 2010;55:759–839.
[47] Liu MC, Du XH, Lin IC, Pei HJ, Huang JC. Intermetallics 2012;30:30–4.
[48] Zhang JY, Wu K, Zhang P, Wang RH, Liu G, Zhang GJ, et al. J Appl Phys 2012;111:113519.
[49] Shi Y, Falk ML. Phys Rev B 2006;73:214201.
[50] Cheng YQ, Cao AJ, Sheng HW, Ma E. Acta Mater 2008;56:5263–75.
[51] Jang D, Greer JR. Nat Mater 2010;9:215–9.
[52] Jang D, Gross CT, Greer JR. Int J Plast 2011;27:858–67.
[53] Shi Y, Falk ML. Phys Rev Lett 2005;95:095502.
[54] Chen CQ, Pei YT, De Hosson JTM. Acta Mater 2010;58:189–200.
[55] Arman B, Brandl C, Luo SN, Germann TC, Misra A, Cagin T. J Appl Phys 2011;110:043539.
[56] Budrovic Z, Van Swygenhoven H, Derlet PM, Van Petegem S, Schmitt B. Science 2004;304:273–6.
[57] Yamakov V, Wolf D, Phillpot SR, Mukherjee AK, Gleiter H. Nat Mater 2004;3:43–7.
[58] Pan D, Inoue A, Sakurai T, Chen MW. Proc Natl Acad Sci USA 2008;105:14769–72.
[59] Yu Q, Shan Z, Li J, Huang X, Xiao L, Sun J, et al. Nature 2010;463:335–8.
[60] Schuh CA, Lund AC, Nieh TG. Acta Mater 2004;52:5879–91.
[61] Pauly S, Gorantla S, Wang G, Kühn U, Eckert J. Nat Mater 2010;9:473–7.
[62] Lewandowski JJ, Greer AL. Nat Mater 2006;5:15–8.
[63] Lee SW, Huh MY, Chae SW, Lee JC. Scripta Mater 2006;54:1439–44.
[64] Johnson WL, Samwer K. Phys Rev Lett 2005;95:195501.
[65] Debenedetti PG, Stillinger FH. Nature 2001;410:259–67.
[66] Courtney TH. Mechanical behavior of materials. Long Grove: Waveland Press; 2000.
[67] Bobylev SV, Mukherjee AK, Ovid'ko IA. Scripta Mater 2009;60:36–9.
[68] Johnson WL, Demetriou MD, Harmon JS, Lind ML, Samwer K. MRS Bull 2007;32:644–50.
[69] Mayr SG. Phys Rev Lett 2006;97:195501.
[70] Ichitsubo T, Matsubara E, Yamamoto T, Chen HS, Nishiyama N, Saida J, et al. Phys Rev Lett 2005;95:245501.